

Arctic-XBeach: A Python-Based Thermo-Morphodynamic Model for Arctic Permafrost Coastal Erosion

Kees Nederhoff¹, Kevin H. de Brujin², Carola Seyfert³, Li Erikson⁴, Stuart Pearson², Robert McCall³, Ferdinand K. J. Oberle⁴, and Tom Ravens⁵

¹Deltas USA: 8601 Georgia Ave 508, Silver Spring, MD 20910

²Delft University of Technology: Stevinweg 1, 2628 CN Delft, The Netherlands

³Deltas, Boussinesqweg 1, 2629 HV Delft, The Netherlands

⁴U.S. Geological Survey - Pacific Coastal and Marine Science Center, Santa Cruz, CA, USA

⁵University of Alaska Anchorage: 3211 Providence Drive, EIB 301P Anchorage , AK 99508

Correspondence: Kees Nederhoff (kees.nederhoff@deltas-usa.us)

Abstract. Climate warming is leading to the erosion of Arctic permafrost coastlines at accelerating rates, with erosion up to 20 m yr⁻¹ along the Alaska Beaufort Sea. However, accurate predictions of this erosion require coupling thermal permafrost dynamics with coastal hydro-morphodynamics, and current models are either computationally prohibitive for long-term simulations or omit important physical processes. Here, we introduce Arctic-XBeach, an open-source Python-based modeling framework that couples the morphodynamic model XBeach to a one-dimensional enthalpy-based thermal module. In contrast to previous implementations, Arctic-XBeach uses an event-driven decoupling approach: the thermal module continuously calculates active layer evolution, while XBeach is only activated during simulated storms when thawed sediment becomes available for erosion. This decreases computational cost by more than XXX% compared to continuous coupling. We validate the model with observations from Barter Island, Alaska, for the period 1980–2010 by reproducing observed patterns in soil temperature profiles (RMSE < 1.3 °C) and bluff retreat driven by thermal denudation (RMSE < XXX m). Arctic-XBeach can be used to run seasonal-to-decadal simulations of permafrost coastal change and offers a modular framework to incorporate additional Arctic-specific processes.

1 Introduction

Permafrost covers more than 30% of the world's coastline, shaping Arctic environments and making these shores vulnerable to climate change (Lantuit et al., 2012). Arctic coasts are either lithified (rock-dominated) or unlithified (sediment-dominated). Unlithified coastlines, typically composed of ice-rich silts and sands, are most at risk of erosion because the warming environment has thawed and weakened coastal sediments. A sediment grain on the Arctic coast is typically locked in place by seasonal ice or permafrost and thawing of that ice/permafrost is a prerequisite for later removal. The warming of the Arctic environment has led to accelerating coastal permafrost thaw, contributing to the increased observed erosion rates. The warming has also led to reduced sea ice and increased wave energy at the coast, which also contributes to the erosion (Overduin et al., 2014; Jones et al., 2020). While Arctic coastal erosion rates in the historic period (1850-1940) averaged about 1 m/year (Nielsen et al.,

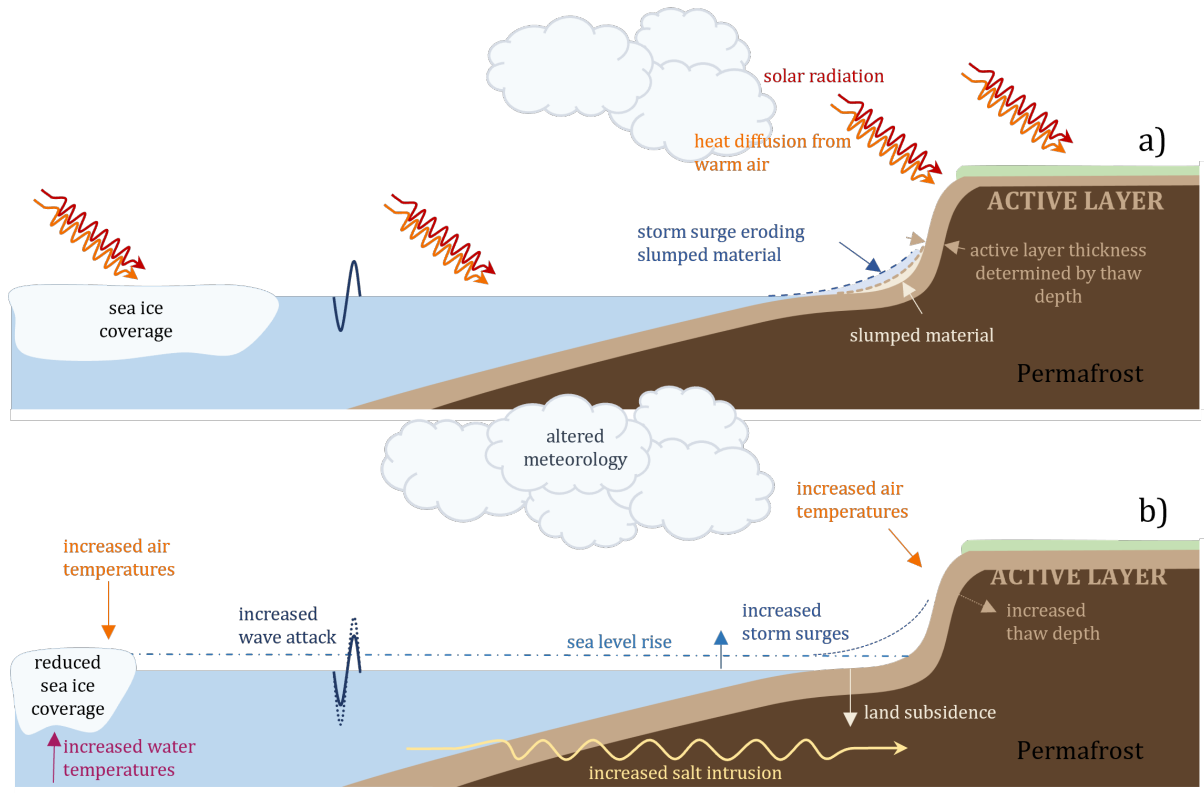


Figure 1. a) Schematisation of the process of coastal erosion, specifically thermal denudation. b) Changes in the process due to climate change. If deeper layers start to thaw they become more susceptible to erosion. Thicker active layers lead to more slumping, and increased storm surges (increase both in number and intensity) lead to more erosion.

2022), researchers have noted an increase in erosion rate in recent years (Jones et al., 2009), with erosion rates on the Alaska Beaufort Sea as high as 20 m/year (Gibbs and Richmond, 2015). Erosion of these ice-rich coasts threatens infrastructure and ecosystems and mobilizes large amounts of organic carbon, amplifying climate feedbacks (Terhaar et al., 2021).

25 Two principal erosion mechanisms are responsible for much of the permafrost bluff retreat in the Arctic: thermal abrasion and thermal denudation (Ravens and Peterson, 2021). Thermal abrasion – also referred to as niche erosion / block collapse – is predominant in coastal settings lacking a high-elevation beach. During storm surge events, the sea is in direct contact with the coastal bluff, and waves and currents thermally and mechanically cut a niche at its base (Kobayashi and Aktan, 1986). Thus, in the thermal abrasion mechanism, the permafrost thaw is driven by oceanic heat transfer. Typically, the niche depth 30 grows to about 5 or 10 m, undermining the bluff leading to block collapse due to an overturning failure (Hoque and Pollard, 2016). Subsequently, the fallen block erodes both thermally and mechanically (Ravens et al., 2012; Barnhart et al., 2014). In Arctic Alaska, locations experiencing bluff retreat rates on the order of 5 to 25 m/year are likely experiencing thermal abrasion. Ravens et al. (2012) developed a process-based and predictive model of Arctic permafrost bluff retreat due to thermal abrasion.

The model considered 12- or 6-hour blocks of time and developed model-based calculations of nearshore water level, waves, and water temperature. When the water level at the coast was sufficiently high and when there were no fallen blocks before the bluff, the model simulated niche erosion using the Kobayashi and Aktan (1986) model. Block collapse was assumed to occur when the cumulative niche depth reached a specified amount (e.g., 5 or 10 m depth). Barnhart et al. (2014) built on the work of Ravens by considering 1-hour time blocks and by computing the occurrence of block collapse based on geotechnical considerations. More recently, Bull et al. (2020) and Frederick et al. (2021) developed more sophisticated and computationally intensive thermo-mechanical model of the thermal abrasion mechanism, featuring 3D stress / strain fields and a plasticity model for permafrost. However, their very sophisticated approach was perhaps too unwieldy for long-term predictions of coastal retreat.

Thermal denudation, in contrast, features permafrost thaw due to atmospheric heat transfer. Coastal bluffs experiencing thermal denudation are fronted by a relatively high-elevation beach which limits direct contact between the sea and the bluff. The overall thermal denudation mechanism includes two steps: (1) thawing of the bluff face due to solar (shortwave) radiation, longwave radiation, latent heat, and sensible heat fluxes, followed by deposition of the thawed material on the beach face and (2) offshore transport of beach face materials due to storm surge events with aggressive waves. Most coastal bluffs in Arctic Alaska are suffering from thermal denudation, and the bluff retreat rate is typically less than 3 m/year. Kasper et al. (2023) and Ravens et al. (2023) developed a process-based model of the thermal denudation mechanism and applied it to represent bluff retreat at Foggy Island Bay, Alaska. Their work featured the development of a 1D thermal model, which computed the daily thaw depth of the bluff face, and manually placed thawed material on the beach face. The second step, the storm-induced offshore transport of beach face sediments, was simulated with XBeach (Roelvink et al., 2009, 2018). Islam and Lubbad (2022) built on the work of previous researchers by modeling coastal configurations where both thermal abrasion and thermal denudation occurred in parallel. However, their work, which featured the application of XBeach, neglected the contribution of solar (shortwave) radiation, longwave radiation, and latent heat flux.

While significant progress has been made in developing Arctic coastal erosion models in the past couple of decades, the coastal community is still needing an open-source model that is able to represent the relevant heat transfer processes, geotechnical stability, and hydrodynamics – and that is able to generate accurate predictions of Arctic bluff retreat. To achieve this goal, we present Arctic-XBeach, a Python-based, modular modeling system integrating the widely used morphodynamic model XBeach (Roelvink et al., 2009, 2018) with a one-dimensional heat-transfer module for thaw simulation of permafrost. Unlike earlier implementations, which run linked hydrodynamic-morphodynamic and thermal models continuously (Ravens et al., 2023), Arctic-XBeach decouples thermal and morphodynamic calculations. Thermal computations run continuously to track active layer dynamics, while the computationally demanding XBeach model runs only during storms. This strategy enables simulations over seasonal to decadal timescales while preserving critical process interactions. Arctic-XBeach also allows users to integrate more processes, such as variable soil properties or salinity effects, without modifying the foundational structure of the code.

In this first version of Arctic XBeach, we focus on the thermal denudation erosion mechanism. We demonstrate the model's applicability using a case study at Barter Island, Alaska, during the 1980-2010 period when thermal denudation was the dom-

inant erosion mechanism. Finally, we present model performance, limitations, and potential future model extension directions
70 toward Arctic coastal hazard analysis and system modeling.

2 Model Formulation

2.1 Conceptual Framework

The thermo-morphological model Arctic-XBeach integrates a hydrodynamic–morphodynamic module (XBeach; Section 2.2) with a new thermal module (Section 2.3) that is coordinated through a Python-based wrapper, see Figure 3. The thermal module
75 calculates freeze–thaw processes and runs continuously during the simulation, while XBeach is only activated during periods of expected morphodynamic activity. XBeach, implemented in Fortran, takes care of computationally demanding tasks. The Python wrapper is responsible for the coupling logic and includes the thermal model. By activating the XBeach executable only when necessary, the wrapper improves computational efficiency without sacrificing representation of important coastal processes. Information on how the two modules communicate and are coupled using the wrapper is covered in Section 2.4.

80 2.2 Hydrodynamics, waves and sediment (XBeach)

The hydrodynamic-morphodynamic core of Arctic-XBeach is the open-source XBeach model (Roelvink et al., 2009, 2018). XBeach solves the (depth-averaged) nonlinear shallow-water equations coupled with a short-wave action balance, together with sediment transport and continuity (Exner) to compute morphological change. XBeach can be run either in "surfbeat" (infragravity or long-wave resolving) or "non-hydrostatic" (fully wave resolving) mode. Here we use the surfbeat mode, in which
85 short-wave groups are handled statistically using wave action balance, but long waves (infragravity waves) are resolved explicitly within the shallow-water equations. The model dynamically updates the bed profile as a function of sediment transport gradients.

We retain XBeach's standard hydrodynamics and sediment codes, e.g., well-tested formulations for avalanching and wave-induced transport, in Arctic-XBeach. XBeach erodes beaches and barriers by default at all instances where calculated shear
90 stresses exceed the value needed for mobilization of sediment. Our addition is to tie this morphodynamic activity to the active layer depth of the thermal module (see Section 2.3). This ensures that only thawed material can be eroded and, in effect, prevents erosion of sediment during early-season storms when the bluff is frozen. This approach encapsulates the key physics of Arctic permafrost coastlines: seasonal thaw controls sediment availability, and storm-driven hydrodynamics provide the dominant erosive force. By releasing sediment erodibility from rigid hydrodynamic thresholds and relating it to a thermal state,
95 Arctic-XBeach produces more realistic timing and magnitude of erosion on seasonal to decadal runs.

2.3 Thermal model

The thermal module of Arctic-XBeach simulates the evolution of the permafrost ground temperature and as a result the active-layer thickness, which directly constrains the volume of erodible material provided to the morphodynamic module of XBeach.

The primary purpose of the thermal module is to compute the thaw depth that defines the erodibility mask used in the coupled

100 model (see Section 2.2).

2.3.1 Enthalpy and temperature

Because both temperature and phase change of the soil are critical for Arctic coastal erosion, a standard heat-conduction approach is insufficient. Instead, we adopt an enthalpy-based formulation of the transient heat conduction equation with phase change (Hu and Argyropoulos, 1996; Ravens et al., 2023):

$$105 \quad \rho \frac{\partial h}{\partial t} = \frac{\partial}{\partial z} \left(k \frac{\partial T}{\partial z} \right), \quad (1)$$

where ρ is the bulk soil density [kg m^{-3}], h is the enthalpy per unit mass [J kg^{-1}], k is the thermal conductivity [$\text{W m}^{-1} \text{K}^{-1}$], T is the soil temperature [K], t is time [s], and z is the coordinate perpendicular to the bluff face [m].

In this framework, enthalpy is defined as the sum of sensible thermal energy and latent heat associated with the phase change
110 of freshwater pore water, assuming no contributions from pore pressure, salinity, or ice-wedge heterogeneity. The temperature–enthalpy relationship is characterized by three distinct regimes (Figure 2). Initially, as energy is added, the temperature increases approximately linearly with enthalpy until the melting point, T_m , is reached. At this stage, additional energy input is primarily consumed as latent heat to melt the ice in the pore space, and the soil temperature remains nearly constant, representing an isothermal phase-change process. Once the latent heat requirement has been satisfied and all pore ice has melted,
115 further energy input again leads to a rise in soil temperature.

This formulation naturally captures freeze–thaw dynamics and the delay in temperature response during phase change. This enthalpy-based approach resolves the freeze–thaw transition and yields a thaw depth (active-layer thickness). In the coupling, XBeach is only permitted to erode thawed material: the morphodynamic update is masked so that sediment transport and bed change are applied on erodible layers. Without this constraint, bed erosion would occur wherever wave-driven shear exceeds
120 the critical stress, irrespective of whether the material is frozen or not, which produces unrealistically large early-season erosion on permafrost coasts.

Mathematically, this relationship can be expressed as

$$T = \begin{cases} \frac{h}{C_s}, & h < C_s T_m, \\ T_m, & C_s T_m \leq h < C_s T_m + L n_b, \\ \frac{h - (C_s - C_l) T_m - L n_b}{C_l}, & h \geq C_s T_m + L n_b, \end{cases} \quad (2)$$

where L is the latent heat of fusion for water–ice [J kg^{-1}] and n_b is the volumetric soil water content.

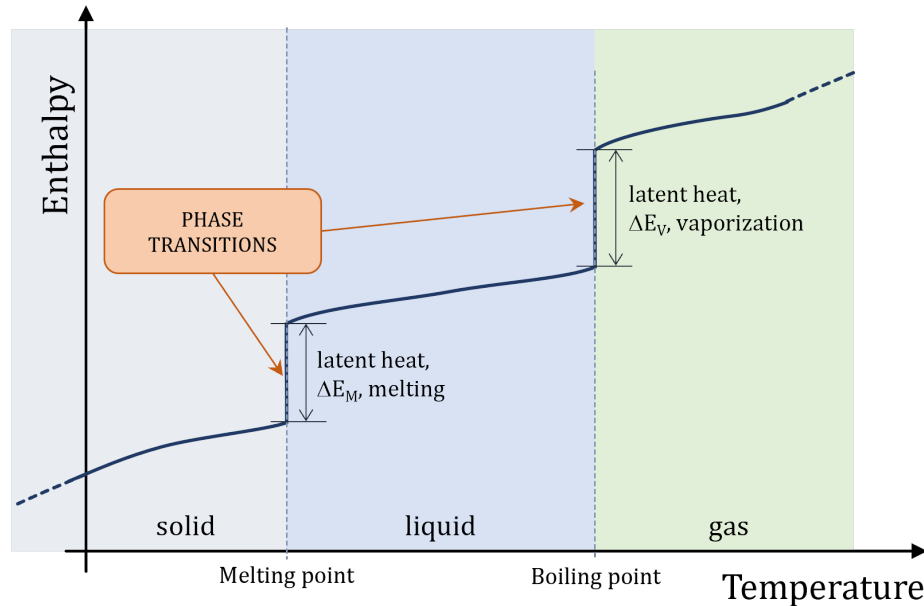


Figure 2. Conceptual enthalpy–temperature relation for a freshwater. Temperature rises with enthalpy until the melting point, where added energy is absorbed as latent heat; after complete melting, temperature increases again. In reality, salinity and pressure can shift the phase-change interval, but those effects are not depicted here.

125 This formulation ensures that the model captures the characteristic thermal behavior of permafrost soils, including the temperature plateau at the melting point during the freeze–thaw transition. In Figure 2, this plateau is visualized as a step in enthalpy at melting point temperature.

2.3.2 Numerical solution and time-stepping

130 The one-dimensional enthalpy-based heat equation is discretized using a Forward-Time Central-Space (FTCS) finite difference scheme, which is second-order accurate in space and first-order accurate in time. Thermal properties, including thermal conductivity and specific heat capacity, are updated at each step to reflect frozen or thawed soil conditions.

The explicit FTCS discretization for cell m at thermal sub-step n is written as:

$$h_m^{n+1} = h_m^n + \frac{k \Delta t}{\rho \Delta z^2} (T_{m-1}^n - 2T_m^n + T_{m+1}^n), \quad (3)$$

135 where h_m^n is the enthalpy at cell m and sub-step n , k is the thermal conductivity [$\text{W m}^{-1} \text{K}^{-1}$], ρ is the soil density [kg m^{-3}], Δz is the vertical grid spacing [m], and Δt is the thermal sub-time step [s].

A Courant number doesn't apply to parabolic (diffusion-type) problems. For the enthalpy equation with an explicit FTCS discretization, stability is assessed via the Fourier number $\text{Fo} = k \Delta t / (\rho C_{\text{eff}} \Delta z^2)$. For the *linear* enthalpy equation (constant properties) the scheme is conditionally stable if $\text{Fo} \leq \frac{1}{2}$. Our formulation is nonlinear because $C_{\text{eff}} = \partial h / \partial T$ varies with phase, so no single equation for stability exists. Instead, we evaluate two limiting linear cases with constant properties: (i) completely frozen soil and (ii) completely thawed soil. In both limits the computed Fourier numbers are well below $\frac{1}{2}$ (e.g., $\text{Fo}_{\text{frozen}} \approx 0.07$ and $\text{Fo}_{\text{unfrozen}} \approx 0.01$ for $\Delta t = 120\text{s}$ and $\Delta z = 0.10\text{m}$ with representative k and C), indicating stability margins and supporting the expectation that the nonlinear case remains stable for the chosen settings. Therefore, in the application case, we use a constant thermal sub-time step $\Delta t = 120\text{s}$ (2 minutes) and a uniform layer thickness $\Delta z = 0.10\text{m}$, which, after some testing, provided convergent and stable results.

2.3.3 Boundary conditions

Boundary conditions in the thermal module are defined at the top (soil surface) and bottom (deep ground) of the one-dimensional thermal column. We implement these boundary conditions using the ghost node method (Coco et al., 2014), which extends the computational domain beyond the physical boundaries to enforce flux-type (Neumann) conditions with second-order spatial accuracy (similar to the rest of the domain).

Grid configuration. The computational grid consists of N interior nodes indexed $m = 0, 1, 2, \dots, N - 1$, where node $m = 0$ represents the physical surface and node $m = N - 1$ represents the bottom boundary. Two additional ghost nodes are introduced: one above the surface (index -1) and one below the bottom (index N). The vertical grid spacing is uniform with $\Delta z = L_z / (N - 1)$, where L_z is the total domain depth (typically 10 m).

155 Ghost-node formulation for Neumann conditions. Suppose the temperature gradient at a boundary node m_b is prescribed through a Neumann condition of the form $\partial T / \partial z|_{m_b} = G$, where the vertical coordinate z is positive downward. To impose this condition with second-order accuracy, we use a three-point central difference centered at the boundary node:

$$\left. \frac{\partial T}{\partial z} \right|_{m_b} \approx \frac{T_{m_b+1} - T_{m_b-1}}{2\Delta z} + O(\Delta z^2), \quad (4)$$

where T_{m_b-1} is the ghost node on the “outside” of the domain and T_{m_b+1} is the first interior node on the “inside”. Substituting (4) into Neumann equation and solving for the ghost-node temperature yields

$$T_{m_b-1} = T_{m_b+1} - 2\Delta z G. \quad (5)$$

This expression is the core of the ghost-node method: once G is specified from the physical boundary condition (e.g., a geothermal gradient or a surface heat flux), the corresponding ghost-node temperature is computed from (5). The factor $2\Delta z$ (rather than Δz) arises from the central difference spanning two grid intervals between $m_b - 1$ and $m_b + 1$, which is essential for second-order accuracy.

Lower boundary condition (geothermal gradient). At the lower boundary ($m_b = N - 1$), we prescribe a fixed geothermal gradient consistent with observations from the North Slope of Alaska (Lowell and Rona, 2005). The imposed gradient is $g_{\text{geo}} = 0.020\text{--}0.030 \text{ K m}^{-1}$. Using the ghost-node formulation, the temperature at the bottom ghost node becomes

$$T_N = T_{N-2} + 2\Delta z g_{\text{geo}}. \quad (6)$$

170 This ensures that the FTCS stencil at node $m = N - 1$ produces a geothermal heat flux consistent with the prescribed gradient.

Upper boundary condition (surface heat flux). At the upper boundary ($m_b = 0$), the boundary condition is expressed as a net surface heat flux $q_n [\text{W m}^{-2}]$, combining convective, radiative, and latent components:

$$q_n = q_{\text{convective}} + q_{\text{radiation}} + q_{\text{latent}}.$$

Using Fourier's law and the ghost-node relation, the surface ghost-node temperature is given directly by

$$175 \quad T_{-1} = T_1 + \frac{2\Delta z}{k} q_n. \quad (7)$$

In the following paragraphs, the individual components of the surface heat flux, convective, radiative, and latent, are described in detail.

180 **Convective heat flux** The convective heat transfer into the frozen soil is a function of a convective heat transport coefficient, denoted by the coefficient h_c , and the temperature difference between the soil and the exterior medium at the interface. The method for determining h_c depends on the external medium, which is either water or air. For air, the approach is much simpler and is given by Equation 8 (Man, 2023).

$$h_{c,\text{air}} = \frac{0.0296 \left(v_w \frac{L_e}{\nu_{\text{air}}} \right)^{4/5} Pr^{1/3} k_{\text{air}}}{L_e}, \quad (8)$$

where $h_{c,\text{air}}$ is the convective heat transfer coefficient for the soil-air interface [$\text{W m}^{-2} \text{K}^{-1}$], v_w is the wind speed at 10 m height [ms^{-1}], L_e is the convective length scale [m], here taken as 0.003 m, ν_{air} is the kinematic viscosity of air [$\text{m}^2 \text{s}^{-1}$], with a typical value of 1.33×10^{-5} , Pr is the Prandtl number [–], typically 0.71 for air, and k_{air} is the thermal conductivity of air [$\text{W m}^{-1} \text{K}^{-1}$], taken as 0.024.

190 Determining convective heat transfer through a soil-water interface, which is subject to waves, is less straightforward. One option is the formulation by Kobayashi et al. (1999). These calculations were developed for breaking waves inducing thermal abrasion of a cliff. However, with the low data availability in the Arctic and the high computational cost of these computations, we made a pragmatic assumption for the convective heat transfer coefficient at the soil water interface, and used a value of 500 $\text{W m}^{-2} \text{K}^{-1}$.

With the convective heat transfer coefficient thus defined for both interfaces (soil/air and soil/water), we can compute the convective heat flux through Equation 9.

$$q_{\text{convective}} = h_{c,\text{air/water}} (T_{\text{soil}} - T_{\text{air/water}}) \quad (9)$$

195 **Radiation flux & solar flux calculator** The radiation flux is the sum of the net influx of shortwave and longwave radiation. Since standard shortwave radiation datasets assume flat terrain, we applied a solar flux calculator to account for inclined surfaces (e.g., permafrost bluffs) following (Kasper et al., 2023). The solar intensity on an inclined surface is:

$$I = I_0 p^{1/\sin A} \sin \theta, \quad (10)$$

200 where I is the solar intensity [W m^{-2}], I_0 is the solar constant, p is the atmospheric transmission coefficient, A is the solar altitude angle, and θ is the angle between incoming radiation and the surface normal (Buffo et al., 1972).

To scale flat-surface radiation to an inclined surface, we used:

$$I_{\text{inclined}} = I_{\text{flat}} \cdot \frac{\sin \theta_{\text{inclined}}}{\sin \theta_{\text{flat}}} = I_{\text{flat}} \cdot r, \quad (11)$$

where r is the enhancement factor, computed dynamically based on slope, aspect, latitude, and time of year.

205 Since longwave radiation is not incident from the sun but from the entire atmosphere, we assumed that the surface angle does not influence the net flux of heat related to longwave radiation. We assumed the same for the surface latent heat flux. Finally, we assumed that the surface fluxes due to shortwave radiation, longwave radiation, and latent heat did not affect the submerged domain.

2.4 Coupling with XBeach

The thermal module numerically updates ground temperature at every thermal time step throughout the simulation to resolve seasonal freeze–thaw cycles. Arctic XBeach checks the forcing conditions and decides whether to invoke the XBeach hydrodynamic–morphodynamic solver. The calculated active layer thickness is put into XBeach as an erodibility mask: thawed material is permitted to erode under wave-driven processes or avalanching, whereas frozen cells are treated as non-erodible. This decoupled strategy improves computational efficiency by not running the XBeach model when early-season storms with frozen bluffs cause minimal erosion. The overall conceptual coupling of Arctic-XBeach is presented in Figure 3. In practice, Arctic XBeach checks whenever XBeach needs to be run at a set time interval. This coupling time step is 1 hour, and the thermal solver’s time step is 120 seconds, which provides approximately 30 thermal updates within every coupling time step.

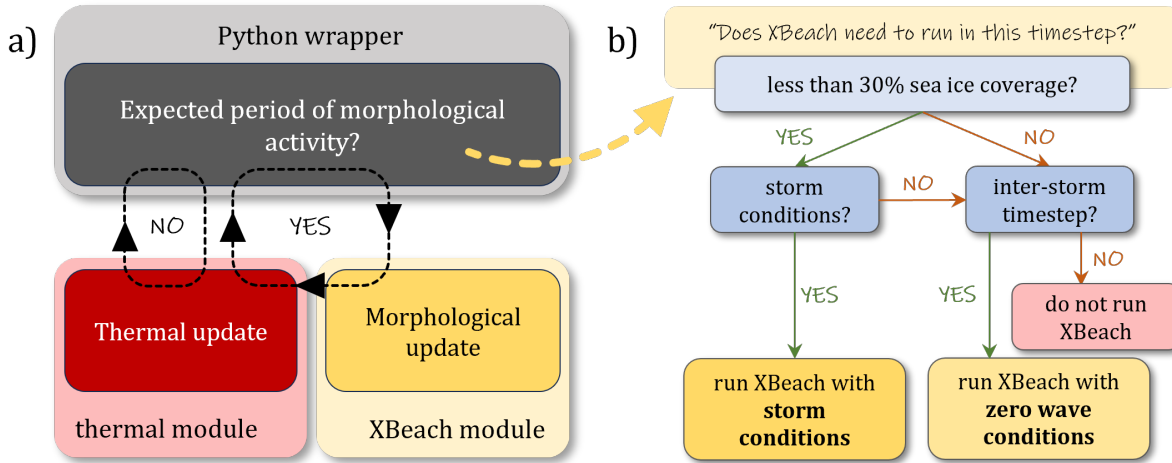


Figure 3. a) Visualisation of the conceptual framework of the python wrapper, including both the XBeach module and the thermal module. No matter whether a morphological update is supplied during a timestep, there will always be a thermal update. b) Visualisation of the decision tree within the python wrapper for when to run the XBeach module, and when not to run it.

2.4.1 XBeach activation logic: when and why to run

The coupling framework relies on a set of physical and pragmatic criteria to decide whether or not to run XBeach. The decision tree implementing the XBeach activation logic is an attempt to reduce computational cost without sacrificing fidelity of the coastal erosion simulation. The Python wrapper module facilitates this activation based on the following three criteria:

220

- **Sea ice presence:** When the sea ice coverage is above a threshold (default: 85%), wave forcing is deemed negligible and XBeach is not activated. This reflects the limitation of the outputs of most global climate models, which do not supply hydrodynamic data above this threshold.
- **Storm-driven activation:** Storm periods are identified from the estimated run-up. In this work, we are utilizing the empirical relation by Stockdon et al. (2006) and compare it to a threshold specified by the user. In case the estimated run-up is greater than the threshold, XBeach is activated to simulate potential morphological changes. This choice is deliberate since we want to only run XBeach during conditions that can remove slumped material from the beach and accelerate erosion at the bluff toe. If $R_{2\%}$ remains below the toe, wave-driven erosion is unlikely and the morphodynamic step can be skipped. The threshold is typically set to result in on average 10 storm-driven activations per year. Lowering the threshold (more frequent activations) generally increases modeled erosion and runtime, whereas raising it has the opposite effect.
- **Inter-storm interval:** To model bluff collapse not connected to wave forcing, XBeach is run at a regular interval even in the absence of storms. This inter-storm interval (default: 1 week) enables gravity-driven slumping of thaw-weakened

225

230

bluff material using the XBeach morphological routines for avalanching. The intent is to (i) deliver slump debris to
235 the toe between storms, (ii) update the topography and erodibility mask seen by the thermal module, and (iii) provide realistic initial conditions for subsequent storms, when run-up exceeding the toe elevation may entrain and remove the deposit.

These conditions are monitored every coupling time step, but XBeach is only invoked if one or more conditions are met.
This event-driven method results in a significant reduction of the number of XBeach simulations to only several days per
240 calendar year. For example, by activating XBeach only during morphologically active periods (typically 3 days per year), the computational cost is reduced by more than 99% relative to continuous year-round simulation.

2.4.2 Thaw Depth Calculation

The phase distribution in the ground determines the erodible layer thickness conveyed to XBeach and the thermal soil parameters (e.g., thermal conductivity k and heat capacity C). The thermal soil conditions are phase-dependent and adapted
245 dynamically by the thermal module through the enthalpy-temperature relationship (Equation 1).

To obtain the thaw depth, used as the erodible layer in XBeach, we transform the calculated thaw interface perpendicular to the ground surface into a vertical coordinate system of XBeach. This transformation is needed specifically in cells with an inclined ground surface, where the thaw depth vector is inclined as well, and can therefore not be expressed with the vertical XBeach coordinate only. For each 1D column, we compute the first cell for which the temperature is below the melting
250 point T_m , and connect these cells by a line approximately parallel to the ground surface, to obtain a piecewise linear thaw interface. The vertical depth of thaw at each surface node was subsequently determined as the vertical distance from the surface downwards to this interface.

In early winter, a shallow layer of frost might overlie previously thawed soil, hiding otherwise erodible material below. To counteract this, we used a *thaw threshold*: a minimum frozen thickness below which the frozen layer is treated as negligible.
255 If the frozen depth from the surface is less than this threshold (default: 3 cells, or 0.3 m), the underlying thawed soil remains erodible. This parameter achieves more physically realistic erosion response across freeze-thaw cycles, recognizing that in Arctic coastal settings, shallow surface freezing (< 0.3 m) does not prevent wave action from mobilizing thawed sediments below.

2.4.3 Data Exchange and Model Run

260 When the wrapper decides that XBeach needs to be executed (on the basis of the presence of a storm, small enough sea ice cover, or inter-storm period), the following data exchange takes place:

1. The thaw depth is calculated and transferred from the thermal model to XBeach.
2. XBeach is run with this thaw depth as the bottom of the erodible bed.
3. Finally, XBeach delivers morphological change and recent water levels and these are fed back to the thermal module.

265 This coupling design ensures two-way feedback between thermal and hydrodynamic- processes in an attempt to improve computational efficiency. To initialize realistic subsurface conditions, each model run included a spin-up period of 10 years prior to the analysis window. This additional runtime allowed the thermal model to establish a stable vertical temperature distribution and ensured that deeper soil layers reached near-periodic seasonal cycles. Although equilibrium in the upper and intermediate layers was typically achieved within three to five years, the full 10-year spin-up provided confidence that
270 subsurface thermal memory was adequately represented before storm events were simulated.

3 Application to Barter Island, Alaska

We apply Arctic-XBeach to a segment of the northern permafrost bluff coastline of Barter Island to demonstrate and validate the model. The site is well-documented with rich observational datasets over multiple decades: historical imagery documents a multi-decadal average retreat rate of about 1.6 m yr^{-1} (70-year mean), with episodic peaks reaching 6.6 m yr^{-1} during
275 2012–2013 (Gibbs et al., 2021). Due to the availability of thermal observations along with bathymetric surveys and shoreline position data, Barter Island forms an ideal testbed for testing the capability of the model to reproduce the observed thermal and morphodynamic behavior under varying Arctic forcing conditions.

3.1 Site description

Barter Island is situated off the northern coast of Alaska, in the North Slope Borough at approximately 70.1° N (Figure 4
280 panel A). The island hosts the village of Kaktovik with a population of 283 as per 2020 (United States Census Bureau, 2020). Its northern coastline consists of unlithified granular material typical for most of the Arctic coastal zone (Lantuit et al., 2012)
such as coastlines in Alaska and Russia.

The site displays a bimodal sediment distribution characteristic of permafrost coasts: beach sediment is characterized as coarse sand with a mean diameter of 1.9 mm (Lantuit et al., 2012; Erikson et al., 2020a) while the bluff crest material is
285 significantly finer with a mean diameter of 0.036 mm (coarse silt) (Ferdinand Oberle, personal communication). Coarse sediment within the permafrost bluff suggests that thermal denudation (bluff face thaw and slump) is the primary erosion process, although thermal abrasion events also occur periodically (Ravens and Peterson, 2021).

The coastal environment is characterized by seasonal sea ice cover, which typically breaks up in late June to early July and reforms in October (Gibbs et al., 2021). During the open-water season, the coast is exposed to storm waves predominantly
290 from the northwest to northeast sectors. Inter-annual variability in erosion rates shows a strong correlation with environmental drivers, including wave power, positive degree days for air and sea surface temperature, and the duration of the ice-free season (Gibbs et al., 2021).

3.2 Input data

Initial conditions, boundary conditions, and forcing data are required as inputs for Arctic-XBeach. Initial conditions define
295 the bathymetric profile and initial ground temperature distribution. The boundary conditions include offshore wave forcing

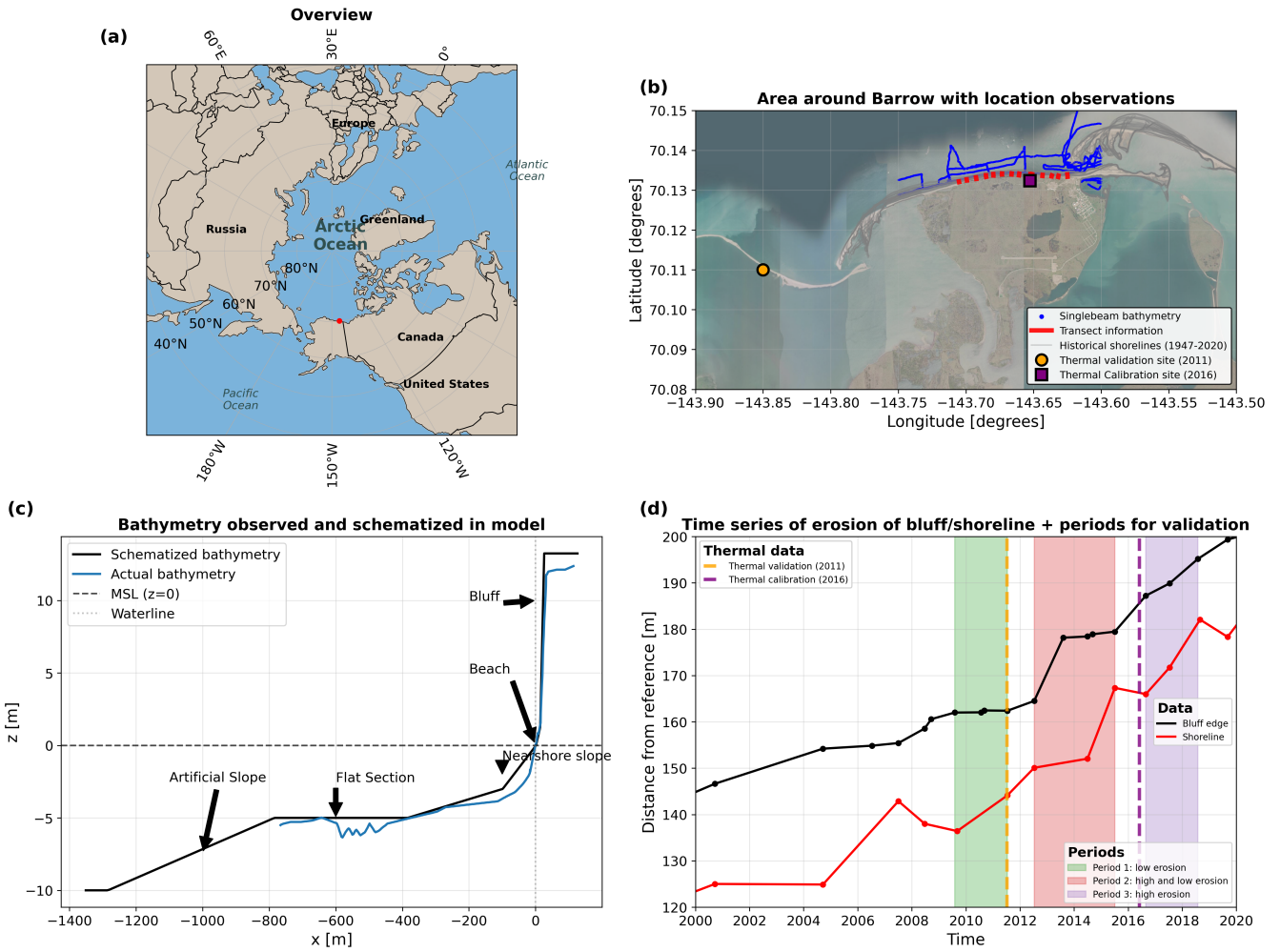


Figure 4. Overview of study domain, observations, and model schematization. (a) Regional map of the Arctic showing the location of the study site near Utqiagvik (Barrow), Alaska (red marker). (b) High-resolution satellite image of the Barrow area with observational datasets used for model setup and evaluation, including single-beam bathymetry profiles (blue), transect information (blue lines), historical shorelines from 1947–2020 (red), and thermal dataset locations used for validation (2011; yellow) and calibration (2016; purple). (c) Cross-shore bathymetry profile based on observations (blue) and its simplified representation used in the Arctic-XBeach model (black). Key geomorphic units are indicated, including the offshore artificial slope, flat nearshore section, beach, nearshore slope, and the coastal bluff. (d) Time series of observed shoreline (black) and bluff-edge (red) positions relative to a fixed reference line from 2000–2020. Shaded regions denote the three erosion regimes used for model evaluation: Period 1 (low erosion), Period 2 (high and low erosion), and Period 3 (high erosion). Vertical dashed lines mark the years used for thermal validation (2011) and thermal calibration (2016).

and lateral thermal boundary conditions at depth. The forcing data consist of time series of atmospheric and oceanographic variables driving thermal and hydrodynamic processes.

3.2.1 Bathymetric transect

We use bathymetric data from (Erikson et al., 2020b), who carried out surveys in 2010 and 2011, yielding a suite of depth soundings and beach-elevation profiles across 29 shore-normal transects. Given the spatial variability of the available measurements and sparse data coverage offshore, we adopted a schematized bathymetric profile for the main model runs informed by these transects. This enables efficient and systematic exploration of the parameter space with reduced uncertainty associated with interpolating sparse observations. This schematized profile consists of: (1) a flat tundra section landward of the bluff, (2) a steep permafrost bluff face, (3) a narrow beach, (4) a nearshore slope extending to approximately 2 m depth, (5) an offshore slope transitioning to deeper water, and (6) a flat offshore section to accommodate the implementation of the equilibrium boundary condition in XBeach (Figure 4 panel C). The profile geometry parameters were constrained by the measured transect and adjusted within the observed ranges during sensitivity analyses.

3.2.2 Initial ground temperature distribution

Initial soil temperature profiles were obtained from ERA5 reanalysis data (Hersbach et al., 2020) that provides soil temperature in four layers (0 to 7, 7 to 28, 28 to 100, and 100 to 289 cm depth) on a 0.25 °grid. The layer center temperatures were taken as the nodal values, which were linearly interpolated to produce a continuous initial profile for the vertical grid of the thermal model.

ERA5 soil temperatures have considerable systematic biases with respect to in situ observations at Barter Island. Therefore, we used a spin-up period to reduce sensitivity to initial condition uncertainties. Simulations of several annual cycles were performed and checked for convergence of the temperature field. It was found that differences between consecutive years had fallen below XX.XXX degrees C after about 3-5 years of spin-up, depending on depth. For the calibration and validation runs, we applied a 10-year spin-up period before the analysis period.

3.2.3 Forcing data

Atmospheric and oceanographic forcing was derived from various sources. Surface energy fluxes, namely, shortwave and longwave radiation, sensible and latent heat, were computed from ERA5 hourly data for air temperature, humidity, wind speed, cloudiness, and sea ice concentration. These are the fluxes that drive the upper thermal boundary condition of the soil heat equation. Wave boundary conditions were specified using significant wave height (H_s), peak period (T_p) from ERA5 ocean wave reanalysis (Hersbach et al., 2020). Waves were transformed from the ERA5 grid point to the model's offshore boundary in (ENGELSTAD => xxx). Water levels were specified using water levels from (NEDERHOFF => XXX). Sea ice presence was incorporated through the suppression of wave forcing when ERA5 sea ice concentration exceeded 50% at the model domain. The geothermal heat flux at the lower boundary was calibrated to (0.0212 K m⁻¹).

3.3 Calibration and validation data

3.3.1 Thermal observations

The soil temperature calibration and validation used two observational datasets. The first dataset contains measurements at 17
330 soil layers over a period of a bit over three months (2016-05-31 - 2016-09-14) and was applied for calibration (?). The second
dataset (Erikson et al., 2020a) includes soil temperature at four layers spanning almost three months (2011-07-08 - 2011-09-
27) and was used for validation. A minor anomaly was present in the 2011 record, likely caused by a temporary removal of
the sensors from the soil (Li Erikson, personal communication), which was excluded from the analysis. Both observations are
close the shoreline of Barter Island ((Figure 4 panel B)

335 3.3.2 Shoreline position

Historical shoreline and bluff edge positions were obtained from ?, who digitized coastal positions from aerial imagery spanning
1947-2020. We extracted bluff edge and shoreline positions relative to a fixed offshore baseline (Figure 4 panel D).

We chose the three following time periods for model evaluation with high erosion rate variability:

- Period 1 (2 August 2009-15 July 2011): low erosion period (mean retreat of 0.2 m yr⁻¹) characterized by below average
340 wave power and positive degree days
- Period 2 (from 11 July 2012 to 5 July 2015): Variable erosion period, with a mean retreat of 5.0 m yr⁻¹, with high positive degree days followed by moderate wave activity
- Period 3 (27 August 2016 to 30 July 2018): High erosion period with mean retreat of 4.1 m yr⁻¹; the period was characterized by an extended ice-free season, elevated temperatures, and sustained wave forcing

345 Period 2 was used for coupled model calibration. Periods 1 and 3 were reserved for independent validation. The bluff edge position was extracted from modeled bathymetric profiles by identifying the point of maximum perpendicular distance from a line connecting the landward and seaward profile endpoints.

3.4 Model setup

The model domain extends 100 m landward of the initial bluff crest to almost 1400 m offshore. This extent ensures that
350 the offshore boundary is beyond the zone of significant morphological change, and also allows space for bluff retreat at the landward boundary over multi-year simulations. Variable resolution is used in the computational grid from XBeach to balance accuracy and efficiency. Finer resolution ($\Delta x = 0.5$ m) is applied in the nearshore and beach zone where morphological gradients are steepest and thermal-morphological coupling is most active. The grid spacing increases gradually offshore and onshore to $\Delta x = 2$ m in regions of gentler slopes. The vertical thermal grid extends to 15 m depth, with constant resolution of
355 $\Delta z = 0.20$ m.

XBeach uses an explicit numerical scheme and computes its own time step but was typically in the order of 0.2 s. The thermal model uses a constant time step of 2 minutes (120 seconds). In turn, the thermal model is updated with a revised bathymetry on an hourly basis, which also corresponds to the resolution of the input atmospheric forcing data. This multi-rate time stepping balances computational efficiency with accurate resolution of the different process timescales: wave periods, morphological adjustment and thermal evolution.

Key model parameters are set as follows. XBeach sediment transport parameters have been set largely to their default values, validated for sandy coasts (Roelvink et al., 2009), with only adjustments for parameters where there is field data to inform them (e.g., critical avalanching slope above water of 0.6 and below water of 0.1, grain size to 36 μm) and minor calibration to other parameters. The morphological acceleration factor morfac is set to 1 (i.e., no acceleration) to preserve the correct temporal sequencing of thermal and morphological processes.

3.5 Calibration

We use a two-step calibration strategy. First, we calibrate the standalone thermal model to reproduce observed temperature profiles, in order to reproduce realistic thaw depths prior to coupling with XBeach. Second, we calibrate the coupled Arctic-XBeach model with observed bluff retreat rates. Direct calibration of XBeach alone at Barter Island is not possible since erosion there is tightly controlled by thermal forcing; hydrodynamic forcing only cannot simulate observed morphodynamics without the correct thaw depth input. Since XBeach is a heavily applied coastal model with validated default parameters (e.g. Roelvink et al. (2009)), we largely depend on default parameters for the hydro–morphodynamic module, but minor calibration to the asymmetry and skewness was performed (XXX)

3.5.1 Thermal model

To calibrate the thermal module of Arctic-XBeach, we applied an automatic hyperparameter optimization procedure using Optuna (Akiba et al., 2019). The objective was to minimize the root mean square error (RMSE) between observed borehole soil temperatures (see Section 3.3) and model results. A set of parameters was allowed to vary within predefined ranges (Table 1). These included soil thermal conductivities (frozen and unfrozen), water/ice content, surface flux factors, and key thermodynamic properties. Parameter ranges were based on literature values and expert judgment, but were broadened where uncertainty existed. The model’s response to parameter changes was non-linear and often counterintuitive; for example, reducing the surface flux factor lowered heat input and decreased active layer depth, while shifts in conductivity and water/ice content produced competing effects. Because of this complexity, automated optimization was essential to identify parameter sets that minimized overall error.

Among all calibration runs, the optimal parameter set was identified with the lowest RMSE of 0.126 $^{\circ}\text{C}$ after 50 epochs. This simulation provided the best match to observed soil temperature profiles, ensuring a robust representation of thermal dynamics during the calibration period. The associated parameters are summarized in Table 1, highlighting the balance between soil thermal conductivity, heat capacity, and thaw depth controls.

Table 1. Calibration parameter ranges, rationale, and optimal values (lowest RMSE run) used in the thermal module optimization.

Parameter	Min	Max	Rationale	Calibrated
max_depth [m]	10	30	Deep enough to exceed seasonal damping depth	15
T_{melt} [K]	270.42	275.88	Around 273.15 K, widened for salinity/pressure representation.	274.56
$L_{\text{water/ice}}$ [J kg^{-1}]	267200	400800	Latent heat of fusion $\sim 3.34 \times 10^5$; $\pm 20\%$.	356819
ρ_{water} [kg m^{-3}]	1000	1030	Fresh to slightly saline/near-freezing water conditions.	951
ρ_{ice} [kg m^{-3}]	825.3	1008.7	Centered on 917 with $\pm 10\%$ for porosity/air effects.	922
ρ_{particle} [kg m^{-3}]	2120	3180	Range spans common soil minerals (quartz ~ 2650).	2672
nb_min	0.25	0.78	Broadened due to strong model sensitivity.	0.405
nb_max	0.25	0.90	Broadened due to strong model sensitivity.	0.742
$c_{\text{soil,frozen}}$ [$\text{J m}^{-3} \text{K}^{-1}$]	3.68e6	5.52e6	Frozen soil heat capacity; consistent with mineral soils + ice.	3.72e6
$c_{\text{soil,unfrozen}}$ [$\text{J m}^{-3} \text{K}^{-1}$]	5.60e6	8.40e6	Higher values reflect liquid water content in thawed soil.	7.74e6
$k_{\text{soil,frozen,min}}$ [$\text{W m}^{-1} \text{K}^{-1}$]	0.70	3.24	Frozen soil conductivity; ice-rich to organic-poor endmembers.	2.00
$k_{\text{soil,frozen,max}}$ [$\text{W m}^{-1} \text{K}^{-1}$]	0.70	3.70	Upper bound for anisotropy and high ice content.	3.63
$k_{\text{soil,unfrozen,min}}$ [$\text{W m}^{-1} \text{K}^{-1}$]	0.30	1.60	Unfrozen soil conductivity; organic-rich to mineral soils.	0.678
$k_{\text{soil,unfrozen,max}}$ [$\text{W m}^{-1} \text{K}^{-1}$]	0.48	1.50	Range for saturated mineral soils, k .	0.791
Geothermal gradient [K m^{-1}]	0.020	0.030	Typical Arctic/permafrost gradients ($20\text{--}30 \text{ K km}^{-1}$).	0.0212

3.5.2 Coupled model

To be done

390 4 Results

4.1 Thermal Model Performance

4.1.1 Verification Against Analytical Solutions

To verify the numerical implementation of the thermal solver, we compared model results against analytical solutions for three heat conduction problems shown in Fig. 5. All tests used uniform thermal properties with constant thermal conductivity and
395 volumetric heat capacity with depth, zero geothermal gradient, and initial conditions chosen such that the simulation stayed in single-phase conditions, thereby satisfying the assumptions on which the analytic solution is based.

400 1. **Case 1: Dirichlet warming.** A frozen soil column initially at 250 K was subjected to a constant surface temperature of 270 K. Using frozen soil properties ($k = 2.7 \text{ W m}^{-1} \text{ K}^{-1}$, $C = 4.6 \times 10^6 \text{ J m}^{-3} \text{ K}^{-1}$), the thermal diffusivity is $\alpha = 5.87 \times 10^{-7} \text{ m}^2 \text{ s}^{-1}$, yielding a characteristic penetration depth of $\sqrt{\alpha t} \approx 4.3 \text{ m}$ after one year. The numerical solution closely follows the analytical profile.

2. **Case 2: Dirichlet cooling.** An unfrozen soil column initially at 300 K was cooled by imposing a surface temperature of 280 K. The lower thermal diffusivity of unfrozen soil ($\alpha = 8.57 \times 10^{-8} \text{ m}^2 \text{s}^{-1}$, based on $k = 0.6 \text{ W m}^{-1} \text{ K}^{-1}$ and $C = 7.0 \times 10^6 \text{ J m}^{-3} \text{ K}^{-1}$) results in significantly slower heat propagation, with a penetration depth of only $\sqrt{\alpha t} \approx 1.6 \text{ m}$ after one year. This approximately seven-fold difference in diffusivity compared to frozen soil is clearly reflected in the shallower thermal penetration visible in Fig. 5 (middle panel).

3. **Case 3: Neumann constant flux.** A constant heat flux of 5 W m^{-2} was applied to the surface of an initially uniform frozen soil column at 250 K. Unlike the Dirichlet cases, no surface temperature is prescribed; instead, the surface temperature evolves freely in response to the imposed flux. The analytical solution for semi-infinite media is included too (Carslaw, H. S. and Jaeger, 1959).

410 Numerical solutions for all three cases are in excellent agreement with the respective analytical predictions. The Neumann case provides the most stringent test of the flux boundary condition implementation and resulted in root-mean-square errors of less than 0.015 K for the entire simulation period, with maximum errors of 0.05 K developing only in the final timestep when finite-domain effects become marginally detectable. These findings verify that the enthalpy-based thermal solver implements both Dirichlet-type (temperature) and Neumann-type (flux) surface boundary conditions correctly while accurately capturing 415 diffusive heat transfer dynamics for the full range of thermal properties relevant to frozen and unfrozen permafrost soils.

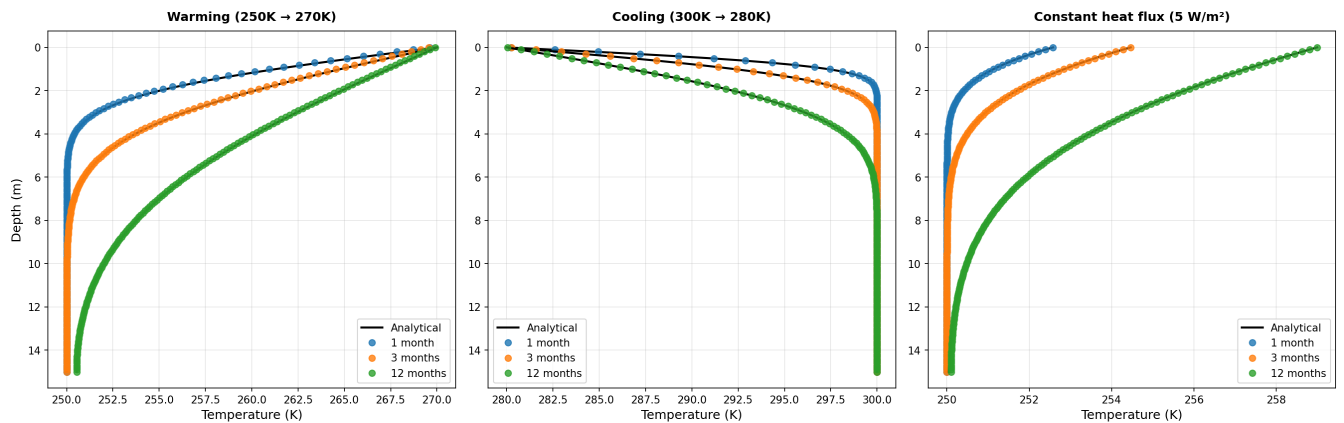


Figure 5. Analytical validation of the thermal solver for three test cases: (left) Dirichlet warming of frozen soil from 250 K to 270 K surface temperature, (middle) Dirichlet cooling of unfrozen soil from 300 K to 280 K surface temperature, and (right) constant Neumann heat flux of 5 W m^{-2} applied to frozen soil. Solid black lines show analytical solutions; coloured markers show numerical results at 1, 3, and 12 months. The slower thermal penetration in the cooling case reflects the lower thermal diffusivity of unfrozen soil.

4.1.2 Temperature Validation

Using the calibrated parameters without further tuning, we validated the thermal module against the independent 2011 record spanning 2011-07-01 to 2011-10-01 (with the brief sensor anomaly removed; see Section 3.3.1). The model reproduces the

observed seasonal warming and its downward propagation into the soil, including the expected damping of amplitude and
420 cooler temperatures with depth.

At the near-surface sensor (top layer), the time series match is close, with an RMSE of 0.47°C and a mean bias of $+0.21^{\circ}\text{C}$ (model slightly warmer). At 2m depth, the RMSE is 1.25°C with a mean bias of -1.21°C (model cooler than observed), consistent with a somewhat stronger attenuation of the thermal signal at depth. The temporal evolution and vertical structure
425 of the warming signal are shown in Figure 6. The combined RMSE of all points combined indicates an error of 1.06°C and a mean bias of -0.72°C (model cooler).

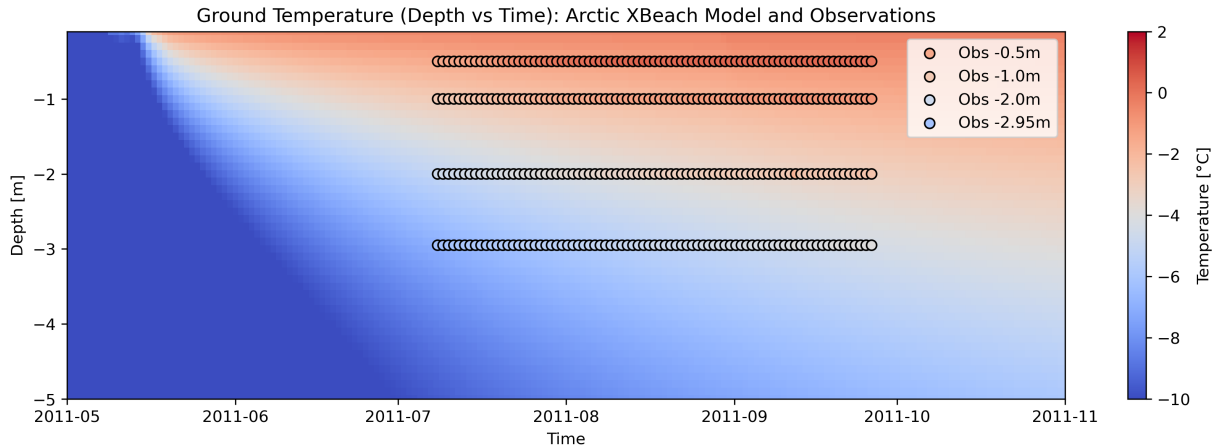


Figure 6. Depth–time map of modeled and observed ground temperature for 2011-05 to 2011-11. The plot shows seasonal warming and its downward propagation.

4.2 Coupled Model Performance

4.2.1 Shoreline evolution (2000-2020)

4.2.2 Storm response events

4.2.3 Morphological change

430 5 Discussion

5.1 Model performance

Arctic-XBeach pushes the boundaries of previous Arctic coastal models by fully utilizing XBeach physics and embedding permafrost thermal dynamics in a modular Python framework. Our approach is flexible, unlike previous couplings implemented

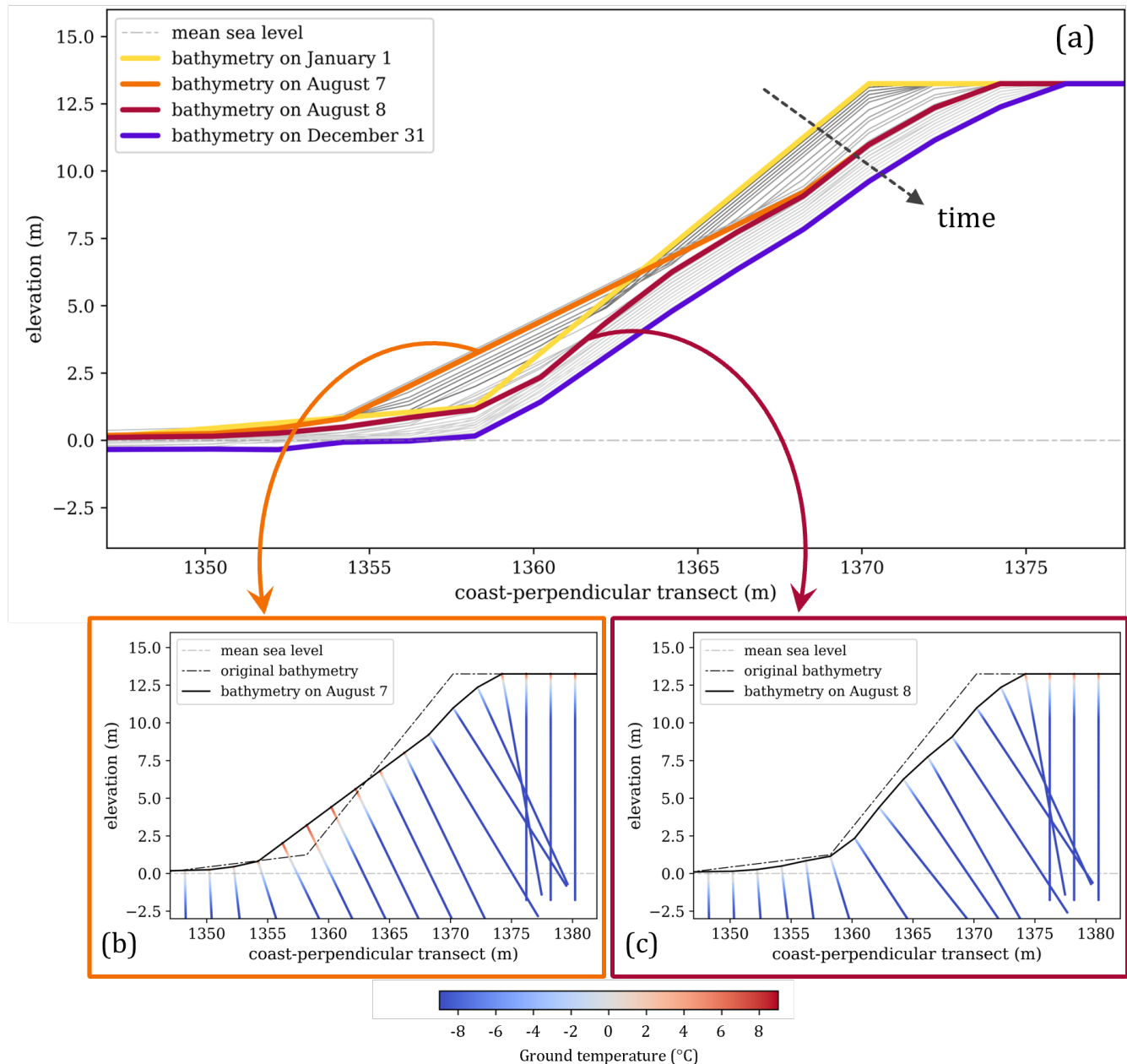


Figure 7. Enter Caption

in Fortran (Ravens et al., 2023): the thermal and hydrodynamic-morphodynamic modules operate independently except via
435 exchange of the thaw depth, easing maintenance and future extensions.

Compared to ArcticBeach v1.0 (Rolph et al., 2022) and the XBeach-submodule approach of Islam and Lubbad (2022), our approach explicitly decouples thermal and morphodynamic time steps for computational efficiency. The thermal module operates at sub-hourly timesteps to resolve heat diffusion and phase change dynamics, while XBeach is invoked only when storm conditions coincide with available thawed sediment, an event-driven approach enabling simulation of annual to decadal
440 timescales with modest computational cost. This efficiency is critical for multi-decadal climate change projections (Nielsen et al., 2022).

The formulations used in Arctic-XBeach consist of an enthalpy-based thermal treatment of the phase transition zone to avoid numerical instabilities when approaching the melting point (Frederick et al., 2021). Analytical validation against ? solutions demonstrates accurate reproduction of both Dirichlet and Neumann boundary conditions in constant-forcing scenarios.

445 [PLACEHOLDER - Computational efficiency, Model skill, Uncertainty]

5.2 Applicability, assumptions and limitations

Arctic-XBeach was developed primarily for the thermo-denudation erosion mechanism, where the gradual thawing of permafrost bluffs leads to slumping and subsequent removal of thawed sediment by wave action. The mechanism described above is dominating at sites with moderate bluff heights and gradual slopes, which includes much of the Alaskan Beaufort Sea coast
450 (Lantuit et al., 2012; Jones et al., 2018).

The 1D thermal transect approach works well in computing vertical temperature profiles and thaw depths, controlling sediment erodibility. However, this approach cannot account for pore water salinity effects on freezing point depression (?), nor explicitly represent ice wedge polygons that create areas with increased weakness that govern block failure (Hoque and Pollard, 2009; Kanevskiy et al., 2013). Moreover, the 1D formulation cannot capture as accurately the lateral heat flow near steep bluff
455 faces or thermal niches, which require at minimum 2DV temperature fields to properly resolve (Frederick et al., 2021)

Although XBeach supports multiple grain size fractions, in our current application of Arctic-XBeach, we assume constant sediment properties of D50, porosity and density within the domain. This simplification reflects that detailed sediment characterization was not available for our study site and most likely also not for other Arctic sites. Arguably, the erodibility is primarily controlled by the frozen/thawed state rather than by grain size. Moreover, XBeach runs in 1D cross-shore mode,
460 which cannot capture alongshore sediment transport processes important for long-term shoreline evolution.

ERA5 reanalysis has atmospheric forcing at a resolution of about 30 km that might not resolve the local meteorological variations. However, ERA5 does show impressive skill at Arctic coastal sites (Hersbach et al., 2020). Downscaling forcing with regional models or at local stations could yield more accurate boundary conditions where this is available. In terms of hydrodynamic forcing, downscaling ERA5 using spectral wave models accounting for sea ice (Nederhoff et al., 2022) is one
465 critical step toward accurate boundary conditions.

Sea ice provides protection against wave action during much of the year. While the model suppresses XBeach activation when ice concentration exceeds a threshold, gradual transitions between ice-free and ice-covered conditions during the shoulder

seasons are not explicitly represented. Inclusion of ice-wave interaction in spectral wave models (Rogers, 2019) would be an improvement, although dynamic wave damping within the XBeach transect when ice is present remains an unresolved
470 challenge.

5.3 Comparison to other models

Several models address thermal abrasion, where wave-driven undercutting creates thermo-erosional niches that destabilize the bluffs. Analytical solutions for the growth of these niches were developed by Kobayashi (1985) and were incorporated into a process-based model by Ravens et al. (2012) for Drew Point. Barnhart et al. (2014) further developed this, embedding bluff
475 stability concepts from Hoque and Pollard (2009), and simulated episodic erosion observed in time-lapse imagery. New 3D finite element analysis was presented by Frederick et al. (2021).

In general, the fully coupled model developed by ? was able to simulate thermo-denudation as well as thermoabrasion with submodels on thawing, slumping, niche growth, and bluff collapse. Some key differences with Arctic-XBeach are: (1) their considerably simpler thermal zone approach versus our explicit enthalpy based temperature evolution, (2) we track thermal
480 state on yearly to decadal timescales such that thaw depths reflect the cumulative heat transfer, and finally, (3) Arctic-XBeach is licensed under the GPL-3.0 license to allow for full reproducibility and community development of this code; it is not obvious that the code of Islam and Lubbad (2022) is publicly available.

Rolph et al. (2022) developed ArcticBeach v1.0 as a simple parameterization for pan-Arctic application within Earth system models, sacrificing process detail for computational efficiency and broad applicability. Arctic-XBeach occupies a middle
485 ground between detailed 3D models that are computationally expensive and site-specific and simple parameterizations that are efficient but with limited physics; event-driven coupling allows multi-decadal simulations maintaining the physical fidelity.

5.4 Future development

We would like to extend the thermal model from 1D to 2DV, where salinity and ice wedge polygons could be explicitly modeled. This change in thermal simulation will be able to represent heterogeneous permafrost properties and preferential thaw
490 pathways, driving block failure patterns more accurately. Another potential development in this direction will be including a niche erosion module using the principles from Kobayashi (1985).

The XBeach cross-shore models cannot represent alongshore sediment transport redistributing the eroded material. We foresee coupling Arctic-XBeach with regional morphodynamic models like Delft3D (Lesser et al., 2004) to simulate coastal evolution over the long term, where alongshore processes (littoral drift, sediment redistribution) and cross-shore processes
495 (thermal denudation, storm erosion) interact. Arctic-XBeach would provide the local erosion rate and sediment flux, while Delft3D would model regional-scale transport and shoreline evolution.social

Arctic coastal erosion releases 5–14 Tg C yr⁻¹ from circum-Arctic coastlines, (Wegner et al., 2015). This flux is expected to double by the end of the century (Nielsen et al., 2022). Arctic-XBeach output of erosion volumes could provide the basis for coupling with carbon flux models in support of integration with Earth system models that currently lack coastal erosion carbon
500 flux representation.

5.5 Societal relevance

Arctic coastal erosion currently presents a variety of threats to Indigenous communities, infrastructure, and cultural heritage. In Alaska, 144 Native communities have been threatened by erosion, flooding, or thawing permafrost, with at least 31 villages in imminent danger (ANTHC (Alaska Native Tribal Health Consortium), 2024). Several communities have initiated relocation
505 or implementing protection, but the high cost of doing this is an obstacle (U.S. Government Accountability Office (GAO), 2009). Compound effects of erosion, subsidence, and sea-level rise may transform 6-8 times more land than erosion alone by 2100 (Creel et al., 2024). Arctic-XBeach has the capability to support decision-making by providing physically based erosion projections that account for coupled thermal–morphological processes unique to permafrost coastlines. The model’s multi-decadal simulation capability enables the assessment of future risk trajectories under different climate scenarios, while
510 the event-driven approach captures the episodic nature of Arctic erosion, determining acute hazard exposure. By making the model openly available, we intend to support research and practical applications by agencies, consultants, and planners protecting Arctic coastal communities and infrastructure.

6 Conclusions

We have developed Arctic-XBeach, a coupled thermo-morphodynamic model for permafrost coastline evolution. By rewriting
515 earlier Arctic erosion codes in a Python framework, we achieve a modular integration of an XBeach-based hydrodynamic model with a 1D heat-transfer (freeze–thaw) model. Governing equations include the shallow-water and Exner sediment equations for XBeach, and a 1D diffusion (enthalpy) equation for soil temperature. The coupling strategy uses the active thaw depth to constrain erosion: only thawed soil can be mobilized by waves. Frozen soil does not erode. Our computational workflow alternates thermal updates with selective storm-driven XBeach runs, greatly improving efficiency. We test the model on a case
520 study of Barter Island, reproducing the expected seasonal erosion patterns. This methodology enables prediction of coastal change over climate-relevant time scales and can be applied to other Arctic sites, always depending on the available background information and calibration data. The Arctic-XBeach code is publicly available on GitHub (XXX). In our future work we want to incorporate alongshore dynamics, more complex failure processes like thermal abrasion, and coupling to regional sea-ice projections.

525 *Code availability.* The Arctic-XBeach code is freely available to anyone and published on Zenodo (XXX) and GitHub (XXX, last access: 1 April 2024).

Appendix A: Solar Calculator

The radiation flux is the sum of the net influx of shortwave and longwave radiation (Equation A1).

$$q_{\text{radiation}} = q_{\text{radiation, shortwave}} + q_{\text{radiation, longwave}} \quad (\text{A1})$$

530 The shortwave radiation flux on a surface depends on the angle that the incoming radiation makes with that surface. Short-wave radiation heat flux data are available for flat surfaces. However, data are not available for an inclined surface (such as a permafrost bluff). To account for bluff inclination, we used a 'solar flux calculator' to scale radiation from a flat surface to an inclined surface (Kasper et al., 2023). For an inclined surface, the amount of incoming radiation was determined using Equation A2 (Buffo et al., 1972).

$$535 \quad I = I_0 p^{1/\sin A} \sin \theta \quad (\text{A2})$$

where,

I = solar intensity [W/m^2] (equals $q_{\text{radiation, shortwave}}$ in Equation A1),

I_0 = solar constant [W/m^2] (radiation at the top of the atmosphere normal to the sun),

p = atmospheric transmission coefficient (depending on altitude, weather, etc.),

540 A = altitude angle [$^\circ$] (angle off of the horizontal with which the sun's rays strike a horizontal surface) = $\arcsin \sin \phi \sin \delta + \cos \phi \cos \delta \cos h$,

ϕ = latitude [$^\circ$],

δ = declination angle [$^\circ$] = $23.5 \times \frac{2\pi}{360} \cos \frac{2\pi}{365} (284 + N)$,

N = current day of the year [-],

h = hour angle [$^\circ$] (varies daily, equaling 0 at 12:00 and π at 00:00, local time),

545 θ = angle between surface and radiation [$^\circ$] = $\sin A \cos \alpha - \cos A \sin \alpha \sin Z - \beta$,

Z = azimuth counter-clockwise from east [$^\circ$] = $AZ + \frac{1}{2}\pi$,

AZ = azimuth counter-clockwise from south [$^\circ$] = $\arcsin \cos \delta \frac{\sin h}{\cos A}$,

Near the solstices, the sun sometimes crosses the east-west line. This happens when $\cos h < \frac{\tan \delta}{\tan \phi}$. If this condition is satisfied, the equation for AZ is modified through Equation A3.

$$550 \quad AZ = \begin{cases} -\pi + |AZ|, & h < 0 \text{ (before 12:00)} \\ \pi - AZ, & h > 0 \text{ (after 12:00)} \end{cases} \quad (\text{A3})$$

The shortwave solar radiation data we used to force the model is defined on the Earth's surface for zero inclination. Equations A4 and A5 respectively represent the intensity of solar radiation on a flat surface, I_{flat} , and intensity of solar radiation on an inclined surface, I_{inclined} .

$$I_{\text{flat}} = I_0 p^{1/\sin A} \sin \theta_{\text{flat}} \quad (\text{A4})$$

555

$$I_{\text{inclined}} = I_0 p^{1/\sin A} \sin \theta_{\text{inclined}} \quad (\text{A5})$$

The atmospheric transmission coefficient is not affected by surface inclination. Hence, we related I_{flat} and I_{inclined} through Equation A6.

$$I_{\text{inclined}} = I_{\text{flat}} \frac{\sin \theta_{\text{inclined}}}{\sin \theta_{\text{flat}}} = I_{\text{flat}} r \quad (\text{A6})$$

560 where,

r = enhancement factor.

We used Equation A6 to compute the intensity of shortwave radiation on an inclined surface based on the intensity of shortwave radiation on a flat surface. The enhancement factor r is a function of surface inclination, day of the year, latitude, etc. (Equations A2 - A5). Figure A1 visualizes the enhancement factor r for several surface inclinations throughout the year
565 for an (almost) north-facing bluff at a latitude of 70 deg. This represents conditions at Barter Island.

We conclude that solar radiation on a north-facing (positively) inclined surface should be reduced for most of the year. Conversely, a negative slope (i.e., a south-facing bluff) leads to a more perpendicular angle between incoming radiation and the surface. This means rays of solar radiation are distributed over a smaller area, which relates to higher solar intensity, and hence an enhancement factor larger than one.

Figure A1. Enhancement factor r (Equation A6) for a bluff facing 88° (clockwise from east) at a latitude of 70°. This direction and latitude is typical for a bluff at Barter Island (Section 3.1). We computed the enhancement factors for a range of different bluff inclinations, for an entire year.

570 *Author contributions.* KN led the writing, model integration, and case study analysis. KdB rewrote Arctic-XBeach in Python, developed the thermal module, and performed the Barter Island case study. TR initiated the Arctic-XBeach concept and developed the original Fortran-based version. CS supported coupling, validation, and project coordination. All authors contributed to discussions and final manuscript revisions.

Competing interests. The contact author has declared that none of the authors has any competing interests

575 *Disclaimer.* Any use of trade, firm, or product names is for descriptive purposes only and does not imply endorsement by the U.S. Government

Acknowledgements. We acknowledge the Deltares SITO-IS research funding as part of the Moonshot 2 – Flooding project, which has provided funding to develop the model and write this paper

References

- 580 Akiba, T., Sano, S., Yanase, T., Ohta, T., and Koyama, M.: Optuna: A Next-generation Hyperparameter Optimization Framework, in: Proceedings of the 25th ACM SIGKDD International Conference on Knowledge Discovery & Data Mining, ACM, <https://doi.org/10.1145/3292500.3330701>, 2019.
- ANTHC (Alaska Native Tribal Health Consortium): Unmet Needs of Environmentally Threatened Alaska Native Villages: Assessment and Recommendations, 2024.
- 585 Barnhart, K. R., Anderson, R. S., Overeem, I., Wobus, C., Clow, G. D., and Urban, F. E.: Modeling erosion of ice-rich permafrost bluffs along the Alaskan Beaufort Sea coast, *Journal of Geophysical Research: Earth Surface*, 119, 1155–1179, <https://doi.org/10.1002/2013JF002845>, 2014.
- Buffo, J., Fritsch, L. J., and Murphy, J. L.: A Second Order Finite-Difference Ghost-Point Method for Elasticity Problems on Unbounded Domains with Applications to Volcanology, 142, 1972.
- 590 Bull, D., Bristol, E., Brown, E., Choens, R., Connolly, C., Flanary, C., Frederick, J., Jones, B., Jones, C., Ward Jones, M., McClelland, J., Mota, A., and Tezaur, I.: Arctic Coastal Erosion: Modeling and Experimentation, pp. 1–270, <https://doi.org/10.2172/1670531>, 2020.
- Carslaw, H. S. and Jaeger, J. C.: Conduction of Heat in Solids, Oxford University Press, 2nd edn., 1959.
- Coco, A., Currenti, G., Del Negro, C., and Russo, G.: A second order finite-difference ghost-point method for elasticity problems on unbounded domains with applications to volcanology, *Communications in Computational Physics*, 16, 983–1009, 595 <https://doi.org/10.4208/cicp.210713.010414a>, 2014.
- Creel, R., Guimond, J., Jones, B. M., Nielsen, D. M., Bristol, E., Tweedie, C. E., and Overduin, P. P.: Permafrost thaw subsidence , sea-level rise , and erosion are transforming Alaska 's Arctic coastal zone, *Proceedings of the National Academy of Sciences (PNAS)*, 121, 1–7, <https://doi.org/10.1073/pnas.2409411121/-DCSupplemental.Published>, 2024.
- Erikson, L., Gibbs, A. E., Richmond, B. M., Jones, B. M., Storlazzi, C. D., and Ohman, K.: Modeled 21st century storm surge, waves, 600 and coastal flood hazards and supporting oceanographic and geological field data (2010 and 2011) for {Arey} and {Barter} {Islands}, {Alaska} and vicinity, <https://doi.org/10.5066/P9LGYO2Q>, 2020a.
- Erikson, L., Gibbs, A. E., Richmond, B. M., Storlazzi, C. D., Jones, B. M., and Ohman, K. A.: Changing Storm Conditions in Response to Projected 21st Century Climate Change and the Potential Impact on an Arctic Barrier Island – Lagoon System — A Pilot Study for Arey Island and Lagoon , Eastern Arctic Alaska, USGS Open-File Report, <https://doi.org/https://doi.org/10.3133/ofr20151193>, 2020b.
- 605 Frederick, J., Mota, A., Tezaur, I., and Bull, D.: A thermo-mechanical terrestrial model of Arctic coastal erosion, *Journal of Computational and Applied Mathematics*, 397, 113 533, <https://doi.org/10.1016/j.cam.2021.113533>, 2021.
- Gibbs, A. and Richmond, B.: National Assessment of Shoreline Change — Historical Shoreline Change Along the North Coast of Alaska , U . S . -Canadian Border to Icy Cape, U.S. Geological Survey Open-File Report 2015–1048, 96 p, 2015.
- 610 Gibbs, A. E., Erikson, L., Jones, B. M., Richmond, B. M., and Engelstad, A. C.: Seven decades of coastal change at barter island, alaska: Exploring the importance of waves and temperature on erosion of coastal permafrost bluffs, *Remote Sensing*, 13, <https://doi.org/10.3390/rs13214420>, 2021.
- Hersbach, H., Bell, B., Berrisford, P., Hirahara, S., Horányi, A., Muñoz-Sabater, J., Nicolas, J., Peubey, C., Radu, R., Schepers, D., Simmons, A., Soci, C., Abdalla, S., Abellan, X., Balsamo, G., Bechtold, P., Biavati, G., Bidlot, J., Bonavita, M., De Chiara, G., Dahlgren, P., Dee, D., Diamantakis, M., Dragani, R., Flemming, J., Forbes, R., Fuentes, M., Geer, A., Haimberger, L., Healy, S., Hogan, R. J., Hólm, E.,

- 615 Janisková, M., Keeley, S., Laloyaux, P., Lopez, P., Lupu, C., Radnoti, G., de Rosnay, P., Rozum, I., Vamborg, F., Villaume, S., and Thépaut, J. N.: The ERA5 global reanalysis, *Quarterly Journal of the Royal Meteorological Society*, pp. 1–51, <https://doi.org/10.1002/qj.3803>, 2020.
- Hoque, A. and Pollard, W. H.: Arctic coastal retreat through block failure, 1115, 1103–1115, <https://doi.org/10.1139/T09-058>, 2009.
- Hoque, A. and Pollard, W. H.: Stability of permafrost dominated coastal cliffs in the Arctic, *Polar Science*, 10, 79–88, <https://doi.org/10.1016/j.polar.2015.10.004>, 2016.
- 620 Hu, H. and Argyropoulos, S. A.: Mathematical modelling of solidification and melting: A review, *Modelling and Simulation in Materials Science and Engineering*, 4, 371–396, <https://doi.org/10.1088/0965-0393/4/4/004>, 1996.
- Islam, M. A. and Lubbad, R.: A Process-Based Model for Arctic Coastal Erosion Driven by Thermodenudation and Thermoabrasion Combined and including Nearshore Morphodynamics, *Journal of Marine Science and Engineering*, 10, <https://doi.org/10.3390/jmse10111602>, 2022.
- 625 Jones, B. M., Arp, C. D., Jorgenson, M. T., Hinkel, K. M., Schmutz, J. A., and Flint, P. L.: Increase in the rate and uniformity of coastline erosion in Arctic Alaska, 36, 1–5, <https://doi.org/10.1029/2008GL036205>, 2009.
- Jones, B. M., Farquharson, L. M., Baughman, C. A., Buzard, R. M., Arp, C. D., Grosse, G., Bull, D. L., Günther, F., Nitze, I., Urban, F., Kasper, J. L., Frederick, J. M., Thomas, M., Jones, C., Mota, A., Dallimore, S., Tweedie, C., Maio, C., Mann, D. H., Richmond, B., Gibbs, A., Xiao, M., Sachs, T., Iwahana, G., Kanevskiy, M., and Romanovsky, V. E.: A decade of remotely sensed observations highlight complex processes linked to coastal permafrost bluff erosion in the Arctic, *Environmental Research Letters*, 13, <https://doi.org/10.1088/1748-9326/aae471>, 2018.
- 630 Jones, B. M., Irrgang, A. M., Farquharson, L. M., Lantuit, H., Whalen, D., Ogorodov, S., Grigoriev, M., Tweedie, C., Gibbs, A. E., Strzelecki, M. C., Baranskaya, A., Belova, N., Sinitsyn, A., Kroon, A., Maslakov, A., Vieira, G., Grosse, G., Overduin, P., Nitze, I., Maio, C., Overbeck, J., Bendixen, M., Zagórski, P., and Romanovsky, V. E.: Arctic Report Card 2020: Coastal Permafrost Erosion, NOAA Arctic Report Card 2020, pp. 1–10, <https://doi.org/10.25923/e47w-dw52>, 2020.
- Kanevskiy, M., Shur, Y., Jorgenson, M. T., Ping, C., Michaelson, G. J., Fortier, D., Stephani, E., Dillon, M., and Tumskoy, V.: Cold Regions Science and Technology Ground ice in the upper permafrost of the Beaufort Sea coast of Alaska, *Cold Regions Science and Technology*, 85, 56–70, <https://doi.org/10.1016/j.coldregions.2012.08.002>, 2013.
- 635 Kasper, J., Erikson, L., Ravens, T., Bieniek, P., Engelstad, A. C., Nederhoff, K., Duvoy, P., Fisher, S., Brown, E. P., Man, Y., and Reguero, B.: Central Beaufort Sea Wave and Hydrodynamic Modeling Study Report 1: Field measurements and model development, Report 1:, 2023.
- Kobayashi, N.: Formation of Thermoerosional Niches into Frozen Bluffs due to Storm Surges on the Beaufort Sea Coast, *Journal of Geophysical Research*, <https://doi.org/10.1029/JC090iC06p11983>, 1985.
- Kobayashi, N. and Aktan, D.: Thermoerosion of Frozen Sediment Under Wave Action, *Journal of Waterway, Port, Coastal, and Ocean Engineering*, 112, 140–158, [https://doi.org/10.1061/\(asce\)0733-950x\(1986\)112:1\(140\)](https://doi.org/10.1061/(asce)0733-950x(1986)112:1(140)), 1986.
- 640 Kobayashi, N., Vidrine, J., Nairn, R., and Solomon, S.: Erosion of Frozen Cliffs due to Storm Surge on Beaufort Sea Coast, *Journal of Coastal Research*, pp. 332–344, <https://www.jstor.org/stable/4298946>, 1999.
- Lantuit, H., Overduin, P. P., Couture, N., Wetterich, S., Aré, F., Atkinson, D., Brown, J., Cherkashov, G., Drozdov, D., Forbes, D. L., Graves-Gaylord, A., Grigoriev, M., Hubberten, H.-W., Jordan, J., Jorgenson, T., Ødegård, R. S., Ogorodov, S., Pollard, W. H., Rachold, V., Sedenko, S., Solomon, S., Steenhuisen, F., Streletskaia, I., and Vasiliev, A.: The Arctic Coastal Dynamics Database: A New Classification Scheme and Statistics on Arctic Permafrost Coastlines, *Estuaries and Coasts*, 35, 383–400, <https://doi.org/10.1007/s12237-010-9362-6>, 2012.

- Lesser, G. R., Roelvink, D., van Kester, J., and Stelling, G. S.: Development and validation of a three-dimensional morphological model, *Coastal Engineering*, 51, 883–915, <https://doi.org/10.1016/j.coastaleng.2004.07.014>, 2004.
- Lowell, R. and Rona, P.: TECTONICS | Hydrothermal Activity, in: Encyclopedia of Geology, edited by Selley, R., Cocks, L., and Plimer, I., 655 pp. 362–372, Elsevier, Oxford, ISBN 978-0-12-369396-9, <https://doi.org/10.1016/B0-12-369396-9/00126-X>, 2005.
- Man, Y.: The Effect of Snow Deposition on Soil Temperature Profile in the Arctic, University of Alaska Anchorage ProQuest Dissertations & Theses, 2023.
- Nederhoff, K., Erikson, L., Engelstad, A., Bieniek, P., and Kasper, J.: The effect of changing sea ice on wave climate trends along Alaska's central Beaufort Sea coast, *The Cryosphere*, 16, 1609–1629, <https://doi.org/10.5194/tc-16-1609-2022>, 2022.
- 660 Nielsen, D. M., Pieper, P., Barkhordarian, A., Overduin, P., Ilyina, T., Brovkin, V., Baehr, J., and Dobrynin, M.: Increase in Arctic coastal erosion and its sensitivity to warming in the twenty-first century, *Nature Climate Change*, 12, 263–270, <https://doi.org/10.1038/s41558-022-01281-0>, 2022.
- Overduin, P. P., Strzelecki, M. C., Grigoriev, M. N., Couture, N., Lantuit, H., St-Hilaire-Gravel, D., Günther, F., and Wetterich, S.: Coastal changes in the arctic, Geological Society Special Publication, 388, 103–129, <https://doi.org/10.1144/SP388.13>, 2014.
- 665 Ravens, T., Henke, M., and Ferreira, C. M.: ARCTIC COASTAL STORMS, UNIQUE IN CHARACTER AND IMPACT, *Coastal Sediments* 2023, pp. 2434–2461, https://doi.org/10.1142/9789811275135_0223, 2023.
- Ravens, T. M. and Peterson, S.: Geologic Controls on Erosion Mechanism on the Alaska Beaufort Coast, 9, 1–8, <https://doi.org/10.3389/feart.2021.693824>, 2021.
- Ravens, T. M., Jones, B. M., Zhang, J., Arp, C. D., and Schmutz, J. A.: Process-Based Coastal Erosion Modeling for Drew Point , North 670 Slope , Alaska, pp. 122–131, [https://doi.org/10.1061/\(ASCE\)WW.1943-5460.0000106.](https://doi.org/10.1061/(ASCE)WW.1943-5460.0000106.), 2012.
- Roelvink, D., McCall, R., Mehvar, S., Nederhoff, K., and Dastgheib, A.: Improving predictions of swash dynamics in XBeach: The role of groupiness and incident-band runup, *Coastal Engineering*, 134, 103–123, <https://doi.org/10.1016/j.coastaleng.2017.07.004>, 2018.
- 675 Roelvink, J., Reniers, A. J. H. M., Van Dongeren, A., van Thiel de Vries, J. S. M., McCall, R. T., Lescinski, J., Roelvink, D., Reniers, A. J. H. M., Van Dongeren, A., van Thiel de Vries, J. S. M., McCall, R. T., and Lescinski, J.: Modelling storm impacts on beaches, dunes and barrier islands, *Coastal Engineering*, 56, 1133–1152, <https://doi.org/10.1016/j.coastaleng.2009.08.006>, 2009.
- Rogers, W. E.: Implementation of Sea Ice in the Wave Model SWAN, 2019.
- Rolph, R., Overduin, P. P., Ravens, T., Lantuit, H., and Langer, M.: ArcticBeach v1.0: A physics-based parameterization of pan-Arctic coastline erosion, *Frontiers in Earth Science*, 10, 1–19, <https://doi.org/10.3389/feart.2022.962208>, 2022.
- Stockdon, H. F., Holman, R. A., Howd, P. A., and Sallenger, A. H.: Empirical parameterization of setup, swash, and runup, *Coastal Engineering*, 53, 573–588, <https://doi.org/10.1016/j.coastaleng.2005.12.005>, 2006.
- Terhaar, J., Lauerwald, R., Regnier, P., Gruber, N., and Bopp, L.: Around one third of current Arctic Ocean primary production sustained by rivers and coastal erosion, *Nature Communications*, 12, 1–10, <https://doi.org/10.1038/s41467-020-20470-z>, 2021.
- United States Census Bureau: 2020 Population and Housing State Data for Whatcom County, WA. <http://censusreporter.org/profiles/05000US53073-whatcom-county-wa>. Accessed 11 July 2022., <http://www.bayareacensus.ca.gov/index.html>, 2020.
- 685 U.S. Government Accountability Office (GAO): Alaska Native Villages: Limited Progress Has Been Made on Relocating Villages Threatened by Flooding and Erosion, 2009.
- Wegner, C., Bennett, K. E., Vernal, A. D., Forwick, M., Fritz, M., Heikkilä, M., Łącka, M., Lantuit, H., Moskalik, M., Regan, M. O., Pawłowska, J., Rachold, V., Vonk, J. E., Werner, K., Wegner, C., Bennett, K. E., Vernal, A. D., Forwick, M., Fritz, M., Heikkilä, M.,

- 690 Łącka, M., Lantuit, H., Laska, M., Moskalik, M., Regan, M. O., Pawłowska, J., Promińska, A., Rachold, V., Vonk, J. E., Wegner, C.,
Bennett, K. E., Vernal, A. D., Forwick, M., Fritz, M., Heikkila, M., Lantuit, H., Laska, M., Moskalik, M., and Regan, M. O.: Variability
in transport of terrigenous material on the shelves and the deep Arctic Ocean during the Holocene Variability in transport of terrigenous
material on the shelves and, 8369, <https://doi.org/10.3402/polar.v34.24964>, 2015.